A modeling approach for upscaling gross ecosystem production to the landscape scale using remote sensing data

Thomas Hilker,[1] Nicholas C. Coops,[1] Forrest G. Hall,[2] T. Andrew Black,[3] Baozhang Chen,[3] Praveena Krishnan,[4] Michael A. Wulder,[5] Piers J. Sellers,[6] Elizabeth M. Middleton,[7] and Karl F. Huemmrich[8]

Received 4 December 2007; revised 28 April 2008; accepted 22 May 2008; published 12 July 2008.

[1] Gross ecosystem production (GEP) can be estimated at the global scale and in a spatially continuous mode using models driven by remote sensing. Multiple studies have demonstrated the capability of high resolution optical remote sensing to accurately measure GEP at the leaf and stand level, but upscaling this relationship using satellite data remains challenging. Canopy structure is one of the complicating factors as it not only alters the strength of a measured signal depending on integrated leaf-angle-distribution and sun-observer geometry, but also drives the photosynthetic output and light-use-efficiency (ε) of individual leaves. This study introduces a new approach for upscaling multiangular canopy level reflectance measurements to satellite scales which takes account of canopy structure effects by using Light Detection and Ranging (LiDAR). A tower-based spectro-radiometer was used to observe canopy reflectances over an annual period under different look and solar angles. This information was then used to extract sunlit and shaded spectral end-members corresponding to minimum and maximum values of canopy-ε over 8-d intervals using a bidirectional reflectance distribution model. Using three-dimensional information of the canopy structure obtained from LiDAR, the canopy light regime and leaf area was modeled over a 12 km^2 area and was combined with spectral end-members to derive high resolution maps of GEP. Comparison with eddy covariance data collected at the site shows that the spectrally driven model is able to accurately predict GEP (r^2 between 0.75 and 0.91, $p < 0.05$).

Citation: Hilker, T., N. C. Coops, F. G. Hall, T. A. Black, B. Chen, P. Krishnan, M. A. Wulder, P. J. Sellers, E. M. Middleton, and K. F. Huemmrich (2008), A modeling approach for upscaling gross ecosystem production to the landscape scale using remote sensing data, *J. Geophys. Res.*, *113*, G03006, doi:10.1029/2007JG000666.

1. Introduction

[2] Satellite data will be essential for driving spatially continuous, global-scale carbon cycle models [*Hall et al.*, 1995a]. Satellite-derived estimates of primary production are based on the links between plant physiological properties, specifically the biochemical composition of plant foliage, and the optical properties of leaves. While the remote sensing community has long been limited by the number and width of spectral wave bands available for detection of leaf optical properties, the recent advent of high spectral resolution optical sensors, capable of detecting changes in leaf spectral properties with a high temporal frequency, has encouraged a new phase in global carbon cycle modeling [*Prince and Goward*, 1995], with an eventual goal of forcing these models entirely with satellite data [*Running et al.*, 2004; *Rahman et al.*, 2005]. As one of the most widely applied concepts for estimating plant productivity (also known as gross ecosystem production, GEP), the light-use-efficiency approach of *Monteith* [1972, 1977] expresses GEP as the product of the incident photosynthetically active radiation (PAR) (μmol m^{-2} s^{-1}), defined as solar radiation between 400 and 700 nm wavelengths, the fraction of PAR that is absorbed by the plant canopy (f_{par}) and the efficiency (ε), with which absorbed PAR can be converted into the chemical energy associated with it:

$$GEP = PAR \cdot f_{PAR} \cdot \varepsilon \quad (1)$$

[1] Faculty of Forest Resources Management, University of British Columbia, Vancouver, British Columbia, Canada.
[2] Joint Center for Earth Systems Technology, University of Maryland, Baltimore County, Goddard Space Flight Center, Greenbelt, Maryland, USA.
[3] Faculty of Land and Food Systems, University of British Columbia, Vancouver, British Columbia, Canada.
[4] Atmospheric Turbulence and Diffusion Division, National Oceanic and Atmospheric Administration, Oak Ridge, Tennessee, USA.
[5] Canadian Forest Service (Pacific Forestry Centre), Natural Resources Canada, Victoria, British Columbia, Canada.
[6] Lyndon B. Johnson Space Center, Houston, Texas, USA.
[7] Biospheric Sciences Branch, NASA Goddard Space Flight Center, Greenbelt, Maryland, USA.
[8] Joint Center for Earth Systems Technology, University of Maryland, Baltimore County, Catonsville, Maryland, USA.

0148-0227/08/2007JG000666$09.00

Remotely sensed estimates of PAR are typically derived from top of the atmosphere solar radiances using satellite observations combined with optical modeling [*Eck and Dye*, 1991; *Sellers et al.*, 1995; *Van Laake and Sanchez-Azofeifa*, 2004], while f_{PAR} is regarded as a function of the leaf area index [*Sellers*, 1985] which in turn is closely related to top of the canopy reflectance measurements in the visible and near infrared region [*Tucker*, 1979; *Daughtry et al.*, 1983; *Asrar et al.*, 1984; *Sellers*, 1985, 1987]. Since the mid-1980s, physical approaches have been developed to determine f_{PAR} globally, based on techniques using satellite data [*Tucker and Sellers*, 1986], plot scale field studies [*Asrar et al.*, 1984; *Tucker et al.*, 1981], large field experiments [*Sellers and Hall*, 1992; *Hall et al.*, 1992; *Sellers et al.*, 1997; *Running et al.*, 1999] and theoretical work [*Myneni et al.*, 2002; *Hall et al.*, 1990; *Sellers*, 1985, 1987; *Sellers and Hall*, 1992; *Sellers et al.*, 1996a, 1996b].

[3] Arguably, one of the most challenging components of the Monteith model to be inferred from remote sensing is ε, which is determined by any of a large number of environmental stress factors and as a result, is highly variable in space and time. One way to infer ε from remotely sensed observations is narrow wave band detection of the epoxidation state of a group of leaf-pigments named xanthophylls, responsible for balancing absorption and utilization of light quanta in order to prevent oxidative damage to the photosynthetic apparatus in leaves [*Demmig-Adams et al.*, 1998; *Demmig-Adams and Adams*, 2000]. *Gamon et al.* [1990] demonstrated a principal relationship between the status of these pigments and a narrow wave band absorption feature at 531 nm, which led to the formulation of the photochemical reflectance index (PRI), comparing this absorption feature to a reference band at 570 nm [*Gamon et al.*, 1992, 1993]. Numerous studies demonstrated a logarithmic relationship between ε and PRI (max ε values correspond to min PRI values and vice versa as PRI is negative) at the leaf and stand level and [*Nichol et al.*, 2002] and *Hilker et al.* [2008a] demonstrated that this signal is detectable over a wide range of view and illumination conditions throughout the year.

[4] However, upscaling this relationship through space and time is difficult. A critical component in upscaling PRI measurements is canopy structure [*Rahman et al.*, 2001], as it not only alters the reflected signal by physically changing its strength depending on integrated leaf angle distribution and the sun-surface-sensor geometry [*Barton and North*, 2001], but also drives the photosynthetic output of individual leaves through its effect on canopy light transmittance [*Forseth and Norman*, 1991]. The capacity of passive remote sensing to investigate such structural dependencies is limited, since remotely sensed reflectances are largely dependent on the properties of the top of the canopy, while the contributions of shaded leaves lower in the canopy are harder to quantify [*Hall et al.*, 1992; *Chen et al.*, 2003; *Myneni et al.*, 2002; *Gao et al.*, 2003]. Further, optical remote sensing measures are typically asymptotic with respect to vertically distributed structural attributes such as leaf area, volume, or biomass [*Wulder*, 1998]. As a result, satellite-derived predictions of primary production often model ε as a biome dependent constant, adjusted by simple meteorological variables such as surface temperature and vapor pressure deficit [*Turner et al.*, 2003; *Heinsch et al.*, 2006], rather than attempting to model directly. The inaccuracies inherent in this method are believed to account for many of the differences found between field measured and satellite derived estimates of GEP [*Running et al.*, 2004]. While direct measurements of ε using satellite data hold promise for calculating more accurate estimates of carbon budgets from space [*Grace et al.*, 2007], appropriate methods to facilitate upscaling from leaf and canopy to landscape level will be required.

[5] One way to investigate the interaction between photosynthesis, canopy radiation regime, and canopy structure is to combine high spectral resolution optical remote sensing data with structural information on the canopy obtained from airborne LiDAR. LiDAR is an active remote sensing technique that facilitates direct measurements of the three-dimensional distribution of vegetation canopy components as well as sub-canopy topography, thereby providing high spatial resolution topographic elevation data, and accurate estimates of vegetation height, cover density, and other aspects of canopy structure [*Lefsky et al.*, 2005]. Measurement errors for individual tree heights (of a given species) are typically in the order of less than 1.0 m [*Persson et al.*, 2002] and less than 0.5 m for plot-based estimates of maximum and mean canopy height with full canopy closure [*Næsset*, 1997, 2002; *Magnussen and Boudewyn*, 1998; *Næsset and Økland*, 2002].

[6] In this paper, we investigate the potential of combining high spectral resolution optical remote sensing observations with small footprint LiDAR data to model ε and GEP vertically and horizontally in a forest whose dominant species is Douglas fir (*Pseudotsuga menziesii* (*Mirbel*)). ε was determined from remotely sensed spectra acquired from a permanently established tower-based spectro-radiometer [*Hilker et al.*, 2007], allowing continuous observation of the canopy surface with high spatial and spectral resolution. First, year-round tower-based measurements were decomposed into sunlit and shaded end-members [*Hall et al.*, 1995b; *Asner et al.*, 1998; *Peddle et al.*, 1999; *Asner and Warner*, 2003] using a bidirectional reflectance distribution model [*Roujean et al.*, 1992; *Hilker et al.*, 2008a]. The physiological signal contained in these end-member reflectances was then spatially extrapolated using information about the canopy structure from LiDAR-based measures. Finally, GEP was calculated separately for sunlit and shaded canopies and compared to vertically and horizontally integrated measurements of GEP obtained from CO_2 exchange measurements using the eddy covariance (EC) technique. The goal of our approach was to investigate possibilities for upscaling stand level observations to satellite scales thereby improving our understanding of interactions between canopy radiation regime and photosynthesis.

2. Site Description

[7] The study area is a Canadian Carbon Program flux tower site, located between Courtenay and Campbell River on Vancouver Island, British Columbia, Canada (49°52′7.8“ N, 125°20′6.3” W, tower location) at 350 m mean above sea level. The coniferous forest consists of 80% Douglas fir, 17% western red cedar (*Thuja plicata* Donn ex D. Don) and 3% western hemlock (*Tsuga heterophylla* (Raf.) Sarg.) [*Morgenstern et al.*, 2004] and is considered to be

second-growth stand, planted in 1949, after harvesting of the original stand [*Goodwin*, 1937]. The understorey consists mainly of salal (*Gaultheria shallon* Pursh.), Oregon grape (*Berberis nervosa* Pursh.), vanilla-leaf deer foot (*Achlys triphylla* (Smith) DC), plus various ferns and mosses [*Morgenstern et al.*, 2004]. A 1998 site survey found that the stand density was 1100 stems ha^{-1}, tree height ranged between 30 and 35 m, with an average diameter at breast height (DBH) of 29 cm. *Chen et al.* [2006] found that the effective leaf area index (L_e) was 4.3 m^2 m^{-2} based on measurements using TRAC and LAI-2000 instruments.

3. Methods

3.1. Eddy Flux Measurements

[8] Continuously since 1997, half-hourly fluxes of CO_2 and water vapor were measured at the site using the EC measurement technique [*Morgenstern et al.*, 2004; *Humphreys et al.*, 2006] and data were extracted between 1 April 2006 and 31 March 2007 for this study. EC-fluxes were measured with a three-axis sonic anemometer-thermometer (SAT, model R3, Gill Instruments Ltd., Lymington, UK) and a closed-path CO_2/H_2O infrared gas analyzer (IRGA) (model LI-6262, LI-COR Inc., Lincoln, NE, USA). Net ecosystem exchange (NEE) was calculated as the sum of the half-hourly fluxes of CO_2 and the rate of change in CO_2 storage in the air column between the ground and the EC measurement level (42 m). Incident and reflected photosynthetically active radiation (PAR [μmol m^{-2} s^{-1}]), defined as the photon flux density for the 400–700 nm wavelength band, were measured using up and downward looking quantum sensors (model 190 SZ, LI-COR Inc.), installed above and below the canopy and diffuse PAR was measured using a "sunshine sensor" (model BF3, Delta-T Devices Ltd., Burwell, UK). Gaps in data collection of less than 2 h were filled using linear interpolation. Half-hourly measurements of GEP were calculated using,

$$GEP = NEP + R_d \quad (2)$$

where NEP is the daytime net ecosystem production (NEP = −NEE) and R_d is the daytime ecosystem respiration [*Morgenstern et al.*, 2004], calculated using the annual exponential relationship between nighttime NEE and soil temperature at 5 cm depth. Gaps in GEP were filled using a Michaelis-Menten GEP versus PAR relationship fitted to daytime data when air temperature $T_{Air} > -1$°C. A complete description of the EC-data and processing methods applied can be found in *Morgenstern et al.* [2004], *Humphreys et al.* [2006], and *Jassal et al.* [2007].

3.2. Spectral Measurements

[9] Canopy reflectance measurements were obtained from an automated multiangular spectro-radiometer platform (AMSPEC) installed at a height of 45 m (≈10 m above the tree canopy) on the open-lattice 50-cm triangular flux tower [*Hilker et al.*, 2007]. The instrument features a motor-driven probe that allows observations in a 330° view area around the tower. The probe rotates in 11.5° intervals every 30 s, thereby completing a full rotation every 15 min. A potentiometer attached to the shaft of the motor facilitates exact measurement of the probe's position. At the end of each sweep, the sensor is returned to its original position. The spectro-radiometer used is a Unispec-DC (PP Systems, Amesbury, MA, USA) featuring 256 contiguous bands with a nominal bandwidth of 3 nm and a nominal range of operation between 350 and 1200 nm. To allow sampling under varying sky conditions, canopy reflectance was obtained from simultaneous measurements of solar irradiance and radiance, sampled every 5 s from sunrise to sunset. The upward pointing probe was equipped with a cosine receptor (PP-Systems) to correct sky irradiance measurements for varying solar altitudes. The downward looking probe measured canopy reflectance at a zenith angle of 62° [*Chen and Black*, 1991]. The probe's instantaneous field of view (IFOV) was 20°. The outer diameter of the instrument's footprint was approximately 62 m at canopy height, while the elliptic instantaneous view area of the probe had a major axis of about 17.9 m and a minor axis of about 3.5 m. No observations were made between an azimuth of 220° and 250° (defined from geodetic north) due to obstruction by the tower. Coinciding with the EC observations, reflectance measurements used for this analysis were collected continuously between 1 April 2006 and 31 March 2007. A complete technical description of the instrument and its setup can be found in *Hilker et al.* [2007].

3.3. LiDAR Measurements

[10] LiDAR data were acquired at the site on 8 June 2004, using a Mark II sensor (Terra Remote Sensing, Sidney, British Columbia, Canada) with a spacing density of 0.7 hits per m^2 and a footprint (spot size) of 0.19 m (with survey and system details in Table 1). Separation of vegetation and terrain was carried out using a software package (Terrascan v. 4.006, Terrasolid, Helsinki, Finland) which iteratively classifies LiDAR data into either ground or non-ground returns. Figure 1 provides an overview of the study area covered by LiDAR measurements.

3.4. Modeling the Eddy Flux Footprint

[11] Interpretation of EC-flux measurements over heterogeneous surfaces is largely dependent on the area or flux footprint from which a measurement originates. The typical size of EC-flux footprints ranges from a few hectares to a few square-kilometres [*Schmid and Lloyd*, 1999] depending on atmospheric stability and meteorological conditions [*Leclerc and Thurtell*, 1990]. As a result, the footprint spatial structure varies significantly over different timescales (half-hourly to multiple years) [*Chen et al.*, 2008]. Exact knowledge of the EC-flux footprints is, however, critical when comparing flux tower measured GEP to spatially integrated remote sensing observations over heterogeneous areas. In this study, a published flux footprint model [*Chen et al.*, 2008] was used to predict the EC-flux footprints for given half hour intervals. This algorithm is based on Eulerian advection diffusion [*Kormann and Meixner*, 2001] and defines the EC-flux footprint as the product of the crosswind-integrated footprint and a Gaussian crosswind concentration distribution function [*Chen et al.*, 2008]. The flux footprint estimates were calculated at half hourly time steps for the period from 1 April 2006 to 31 March 2007 with a spatial resolution of 10 m x 10 m covering the 12 km^2 area around the tower. The output of the model is

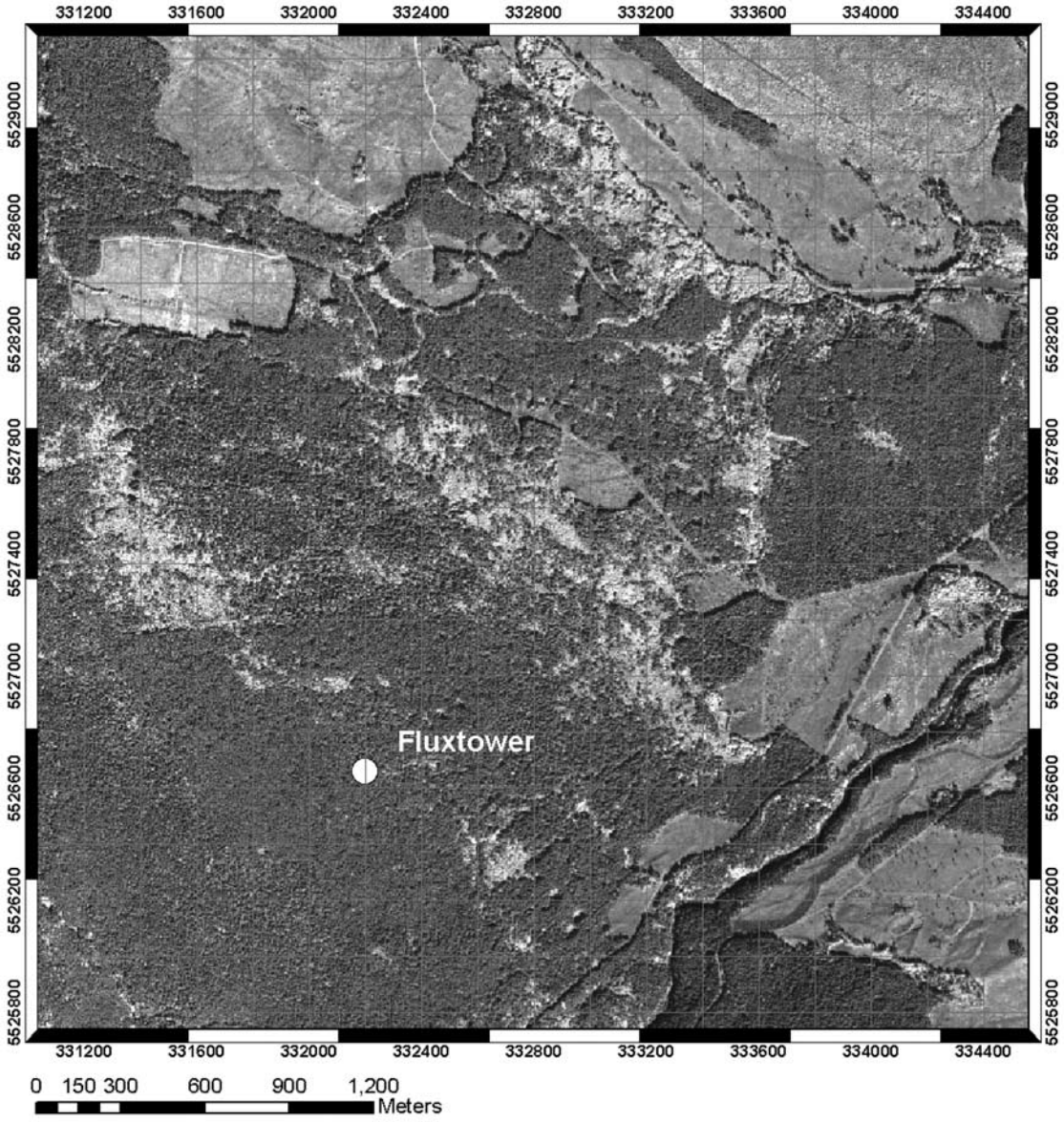

Figure 1. QuickBird satellite image of the study area covered by LiDAR. The total size of the area is approximately 12.5 km^2.

the percent impact each 10 m x 10 m cell within the raster has on the EC-flux measurement per half hour time step.

3.5. End-member Reflectance of PRI

[12] Building upon the theoretical foundation of *Li and Strahler* [1985], *Hall et al.* [1995b] illustrated that multi-angular stand level reflectance signals for a given species can be decomposed into spectral end-members, namely sunlit crown, sunlit background, and shadow. The fraction of area occupied by each of these end-members for a given observation varies as a function of the sun - observer geometry and can be determined using linear mixture modeling if the reflectance for totally sunlit and totally shaded crown and background are known [*Hall et al.*, 1995b; *Asner et al.*, 1998; *Peddle et al.*, 1999; *Asner and Warner*, 2003]. In this study, we simplified this concept by reducing the number of end-members to sunlit and shaded crown components only, as the background reflectance was assumed to make a minimal contribution due to the high canopy density at the study site. Sunlit and shaded end-member reflectances can only be approximated from direct AMSPEC measurements, as the instrument, which has a field of view of approximately 60 m^2, will always observe a mixture of sunlit and shaded canopies. However, it is possible to accurately determine these end-members using a bidirectional reflectance distribution function (BRDF) derived from the AMSPEC acquired spectra. A BRDF describes how land surface reflectance varies with view zenith, solar zenith and azimuth angle [*Barnsley et al.*, 1997; *Gao et al.*, 2003] and is often applied to standardize multiangular reflectance measurements to common viewing geometries. Once a BRDF model is established for a series of multidirectional measurements, reflectance values can be estimated for any possible sun-observer geometry, including

Table 1. LiDAR Parameters

Parameter	Performance
Sensor	Mark II
Laser scan frequency	25 Hz
Laser impulse frequency	40,000 Hz
Laser power	<4 Watt
Maximum scan angle	<20°
Type of scanning mirror	oscillating
Laser beam divergence	<0.5 milliradians
Measurement density	0.5–0.8 hits per sq meter.
Geodetic datum	NAD83
Plotting projection	UTM Zone 10
Airborne platform	Bell 206 Jet Ranger helicopter
Flight altitude above ground	900 m
Flight speed	25–30 m s^{-1}
Version of TerraScan used to classify data	Version 004.006

those for which no measurements were acquired. In terms of a BRDF, the sunlit end-member reflectance corresponds to a geometry where probe is perfectly aligned with the sun being behind it (the so-called BRDF hot spot) while the shaded end-member corresponds to a geometry where sun is located in front of the probe (BRDF dark spot) [*Li and Strahler*, 1985; *Middleton et al.*, 1987; *Li and Strahler*, 1992; *Wanner et al.*, 1995]. The shaded PRI end-member then defines the highest possible photosynthetic performance for a given time interval, while the sunlit PRI end-member defines its lowest performance. *Hilker et al.* [2008a] demonstrated that the PRI reflectance as observed by AMSPEC is a function not only of the sun-observer geometry, but also of the sky condition at the time of measurement and the physiological status of the vegetation canopy observed (i.e., ε). To facilitate accurate modeling of BRDF, geometric effects need to be separated from both leaf physiological effects as well as reflectance effects related to sky conditions. This can be achieved by stratifying spectra into homogeneous subsets of observations with respect to both sky conditions and tower measured ε and subsequently fitting individual BRDF models to each of these strata [*Hilker et al.*, 2008a].

[13] The time period for modeling BRDF needs to be chosen carefully, as a set of spectral observations is required that is large enough to establish a stable BRDF surface [*Los et al.*, 2005; *Hilker et al.*, 2008a] but the time period should not be so long as to incorporate physiological responses in leaves as this may not adequately represent variations in photosynthetic performance over shorter time intervals. In this study, an 8-d period was chosen for calculation of PRI end-members and thus also for calculating GEP, as this interval is also commonly used in satellite products such as the GEP product of the Moderate Resolution Imaging Spectro-radiometer (MODIS) [*Heinsch et al.*, 2006].

3.6. Determining Stand Structural Parameters Using LiDAR

[14] LiDAR data were used to estimate forest stand attributes, including L_e and the probability of canopy gaps within different layers of the forest canopy (P_{gap}). Computation of P_{gap} from the top of the canopy to a given depth into the canopy (z) has been described in detail by *Lovell et al.* [2003] and *Coops et al.* [2007]. For a given cell, P_{gap} can be estimated by summing the total number of LiDAR returns down to z and comparing them to the total number of independent LiDAR pulses (N):

$$P_{gap}(z) = \frac{1 - \sum_{z=j}^{z=z_{\max}} \#z_j}{N} \tag{3}$$

where $\#z_j$ is the number of hits down to a height z above the ground. From P_{gap}, the cumulative projected foliage area index $L(z)$ from the top of the canopy down to a height z can be derived using,

$$L(z) = -\log\left(P_{gap}(z)\right) \tag{4}$$

where the first derivative of $L(z)$ is the apparent foliage density profile [*Lovell et al.*, 2003; *Coops et al.*, 2007]. The effective P_{gap} of a clumped forest canopy at a given time of the day (P_e), can be calculated if $L(z)$ and the solar zenith angle (θ) are known [*Chen*, 1996]:

$$P_e(\theta, z) = \exp\left[\frac{-G_t(\theta)L(z)}{\cos\theta}\right] \tag{5}$$

where $G_t(\theta)$ is the projection coefficient for total PAR transmission approximated as 0.5 [*Chen*, 1996; *Chen et al.*, 2006]. θ was calculated for each 30-min interval using the timestamps from the flux measurements [*Reda and Andreas*, 2004]. Estimates of canopy structure were based on a spatial resolution of 10 m × 10 m, corresponding to the flux-footprint model [*Chen et al.*, 2008].

3.7. Establishing a Spatial GEP Model

3.7.1. Modeling PAR as a Function of θ and z

[15] As a simplifying assumption, the forest canopy is herein modeled as two populations of sunlit and shaded leaves, with photosynthesis driven by the direct and diffuse radiation components, respectively [*Norman*, 1980; *Forseth and Norman*, 1991]. Following this concept, incident PAR at the top of the canopy (Q_{total0}) can be decomposed into direct and diffuse radiation components, measurable using total and diffuse PAR sensors.

$$Q_{total\ 0} = Q_{b0} + Q_{d0} \tag{6}$$

where Q_{b0} is the direct radiation component and Q_{d0} is the diffuse component a the top of the canopy. The direct radiation penetrating the canopy will decrease exponentially as a function of $P_e(\theta,z)$:

$$Q_b(\theta, z) = Q_{b0}P_e(\theta, z) \tag{7}$$

The diffuse radiation component Q_d also extinguishes exponentially through the canopy but the extinction coefficient is assumed to be invariant with solar angle and much smaller than for direct PAR [*Weiss and Norman*, 1985; *Brakke*, 1994; *Smolander and Stenberg*, 2001]. Diffuse radiation is therefore mostly a function of the

canopy density [*Annandale et al.*, 2002] and total PAR per canopy height layer can be calculated using

$$Q(\theta,z) = Q_{b0}P_e(\theta,z) + Q_d(z) \quad (8)$$

3.7.2. Modeling f_{PAR}

[16] The fraction of PAR absorbed per canopy layer ($f_{PAR}(\theta, z)$) varies with the solar zenith angle and canopy depth and is a function of the foliage density profile. Consequently, the amount of foliage intercepted by a light beam at a specific height z can be calculated as

$$f_{PAR}(\theta,z) = f_{PAR0} \times (P_e(\theta,(z-1)) - P_e(\theta,z)) \quad (9)$$

where f_{PAR0} is the total fraction PAR absorbed, P_e (θ, z) is the effective probability of gap at a given height z and P_e (θ, $z - 1$) is the effective probability of gap of the height above it.

3.7.3. Modeling GEP

[17] Using (1), a direct and diffuse GEP component can be computed for each 10 × 10 m cell from the sunlit and shaded end-members of PRI, if the ε related response to a given amount of light is assumed to be constant throughout the canopy:

$$GEP_b(\theta,z) = f(PRI_b) \times f_{PAR}(z) \times Q_b(\theta,z) \quad (10a)$$

$$GEP_d(z) = f(PRI_d) \times f_{PAR}(z) \times Q_d(z) \quad (10b)$$

where PRI_d and PRI_b are the sunlit and shaded end-members of measured PRI reflectance, respectively. While EC-measurements provide a vertically and horizontally integrated bulk canopy estimate of ε over the flux-footprint, the spectral measurements result in end-members of sunlit and shaded PRI. These PRI measurements can be translated into ε values when assuming the horizontal distribution of sunlit and shaded leaves to be constant within the yearly daytime footprint, which is a reasonable approximation due to the homogeneity of the examined forest stand. In order to derive sunlit and shaded values of ε from the PRI end-members, a logarithmic relationship was established between ε and sunlit PRI ($f(PRI_b)$), and ε and shaded PRI ($f(PRI_d)$), and applied to the model, respectively [*Hilker et al.*, 2008a, Figure 2].

[18] Integrating equations (10a) and (10b) over all height intervals (z) from 1 m to the maximum tree height (z_{max}) and over all 10 m × 10 m cells (c) within the study area, yields the total amount of photosynthesis for the direct and diffuse radiation component.

$$GEP_{Ib} = \int_{c=1}^{c=c_{max}} \left(\int_{z=1m}^{z=z_{max}} GEP_b(\theta,z)dz \right) dc \quad (11a)$$

$$GEP_{Id} = \int_{c=1}^{c=c_{max}} \left(\int_{z=1m}^{z=z_{max}} GEP_d(z)dz \right) dc \quad (11b)$$

where GEP_{Id} and GEP_{Ib} are the remotely sensed estimates for the direct and diffuse GEP components, respectively.

3.8. Comparing EC Determined to Remotely Sensed GEP

[19] Estimates of GEP provided by EC-flux data were compared with estimates derived from remotely sensed data as follows: The integrated LiDAR and optical remotely sensed outputs of (10a) and (10b) were weighted according to footprint of each 10 × 10 m cell. The EC-footprint weighted GEP components can be defined as

$$GEP_{Ibw} = \int_{c=1}^{c=c_{max}} \left(\int_{z=1m}^{z=z_{max}} GEP_b(\theta,z)dz \right) \phi(c)dc \quad (12a)$$

$$GEP_{Idw} = \int_{c=1}^{c=c_{max}} \left(\int_{z=1m}^{z=z_{max}} GEP_d(z)dz \right) \phi(c)dc \quad (12b)$$

where $\phi(c)$ describes the footprint per 10 m x 10 m cell (c) and GEP_{Idw} and GEP_{Ibw} are the footprint weighted estimates for the direct and diffuse GEP components, respectively.

4. Results

4.1. PRI End-members

[20] Figure 2 shows the relationship between the sunlit PRI component and tower measured ε and the shaded PRI component and tower measured ε as daily averaged values throughout the one year period. Both PRI end-members reveal a highly significant, nonlinear relationship to tower measured ε, with the strongest correlations found between ε and the sunlit PRI component ($r^2 = 0.91$, $p < 0.05$) while the relationship between ε and the shaded PRI component was $r^2 = 0.86$ ($p < 0.05$). Also, differences between sunlit and shaded PRI end-members (ΔPRI) were highest under conditions where ε was low and became smaller with increasing ε-values.

[21] Figures 3a–3d show sunlit and shaded end-members of PRI, averaged as 8-d values between 1 April 2006 and 31 March 2007, as a function of time (Figure 3a), the ratio of direct to diffuse sky radiation above the canopy (Q) [*Hilker et al.*, 2008b] (Figure 3b), soil moisture (Figure 3c) and atmospheric pressure deficit (Figure 3d). As expected from previous studies conducted at this site [*Hilker et al.*, 2008a], the PRI of shaded leaves was generally larger than that of sunlit leaves, indicating that shaded leaves are exposed to less stress and thus have a higher ε-value than sunlit parts of the canopy. *Hilker et al.* [2008a] showed that the canopy stress level is strongly related to the difference between sunlit and shaded PRI components (ΔPRI). These differences can largely be explained by meteorological variables. The ratio of direct to diffuse sky radiation above the canopy, representing the state of cloudiness, accounted for about 50% of variation in ΔPRI alone ($p < 0.05$) (Figure 3b), while the atmospheric vapor pressure deficit (D) (Figure 3d) explained 39% of variations in ΔPRI ($p < 0.05$). The soil-moisture content explained about 60% of variation in ΔPRI, except during the mid to late summer period (DOY 190–268) when soil moisture content was low. A linearized multiple regression revealed that these three meteorological variables together explained 79% of variation in ΔPRI

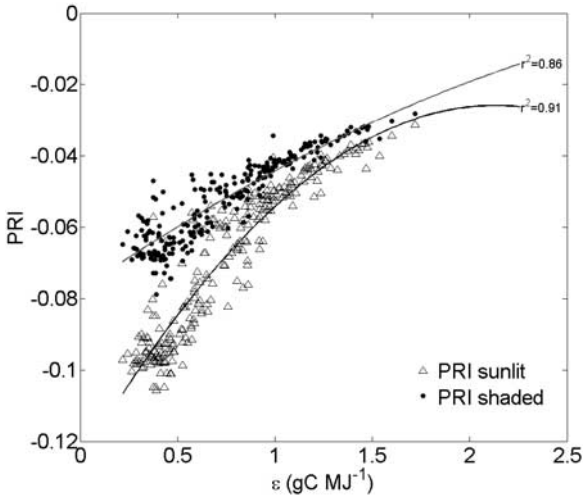

Figure 2. Relationship between sunlit PRI and ε and shaded PRI and ε throughout the study period. The relationship is strongest between the sunlit PRI component and ε ($r^2 = 0.91$, $p < 0.05$), but is still highly significant for the shaded PRI component and ε ($r^2 = 0.86$, $p < 0.05$). The difference between the sunlit and shaded PRI component is highest under conditions, where ε is low.

($p < 0.05$) throughout the year. Differences between sunlit and shaded end-members of PRI were largest in late summer when the canopy underwent significant drought and temperature stress, as well as in late winter, due to snowfall. Minimum differences were found through spring and early summer, when the canopy underwent only moderate stress.

4.2. Determining Stand Structural Parameters Using LiDAR

[22] Figure 4 shows vertical profiles for L_e, P_{Gap} and the sunlit component of GEP for a mature (left column: Figures 4a, 4c, and 4e) and a young (right column: Figures 4b, 4d, and 4f) Douglas-fir dominated forest stand for 28 August, 9:30 A.M. Pacific Standard Time (PST) (solar elevation = 36.4°). The mature stand is adjacent to the flux tower site, while the young stand is located in the northeast of the 12 km^2 area and has a canopy height of 10 m (distance to tower: 1.5 km). L_e (Figures 4a and 4b) and P_e (Figures 4c and 4d) are shown for the mature and young stand respectively. A vertical profile of GEP is shown only for the sunlit GEP component (Figures 4e and 4f), as GEP_d was calculated for all canopy layers as a whole since it was assumed to be independent of within-canopy shading. The sunlit component of GEP diminishes quickly with decreasing height

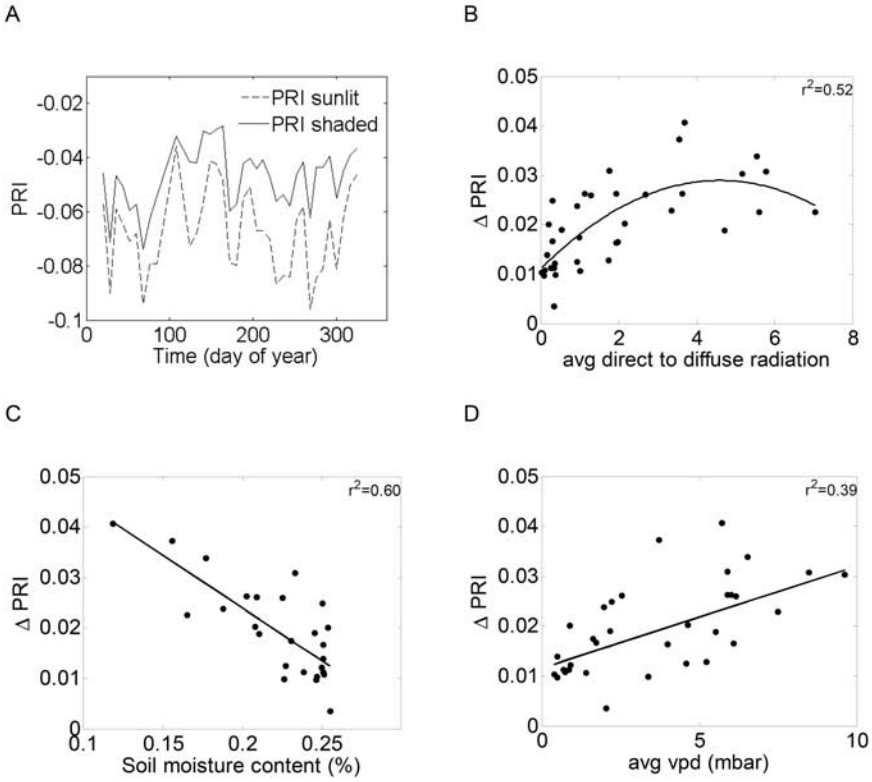

Figure 3. (a) Difference between sunlit to shaded PRI (Δ PRI) over a year computed as 8-d averaged data sets. Sunlit and shaded PRI were calculated using a kernel driven BRDF approach (Ross-Thick Li-Sparse Kernels). Relationship between Δ PRI and (b) 8-d averaged state of cloudiness, expressed as ratio of direct to diffuse radiation, (c) 8-d averaged soil moisture content (%/100 (vol. water content)) (excluding DOY 190–268), and (d) 8-d averaged vapor pressure deficit (in mbar). Multiple regression analysis of all 3 components explained 77% of variation in Δ PRI. (all relationships where established for $p < 0.05$).

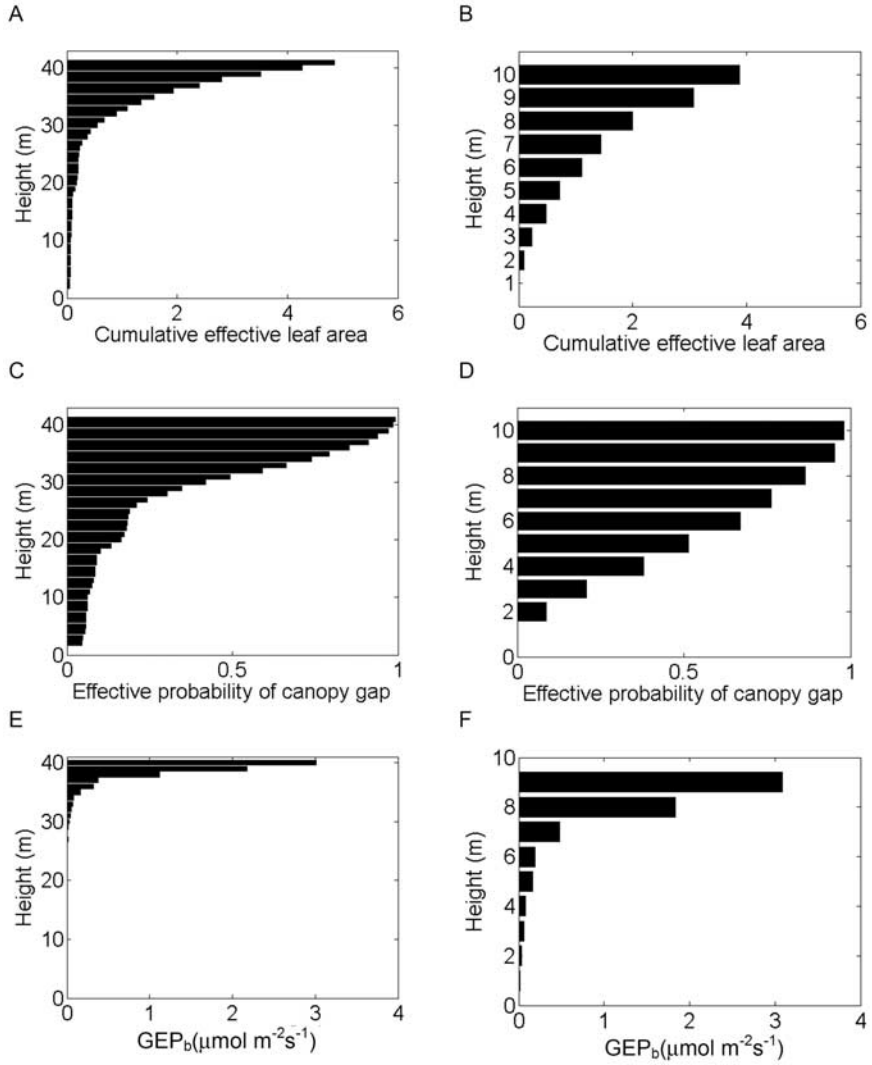

Figure 4. Vertical profile of cumulative leaf area, effective probability of canopy gap and sunlit components of GEP for (a, c, e) a mature and (b, d, f) a young Douglas fir stand as derived from spectral and LiDAR measurements for a given θ (25°). The shaded GEP component has been derived as integrated measurement over all heights as the diffuse radiation component was assumed to be constant throughout the canopy.

since PAR_b is largely absorbed within the top 10 m of the canopy (Figures 4e and 4f).

4.3. Spatial Modeling of GEP

[23] Figure 5 shows the spatial distribution of sunlit GEP for a cloudy (Figure 5a) and a sunny day (Figure 5b). The figure shows the percent coverage of the sunlit GEP component for each 10 m × 10 m cell. The ratio of direct to diffuse radiation was 0.2 and 9, respectively. Differences between sunlit and shaded GEP coverage are most distinct for the sunny day and within younger stands with open spaced regeneration (compare Figure 1), dominated by direct sunlight due to the lack of canopy structure. Diffuse radiation played a larger role in mature forested areas where it dominates the radiation regime in the lower portions of the canopy. On overcast days, diffuse sky radiation provides the majority of incident PAR, and structure-related differences in percent cover as expressed in spectral descriptions using end-members become more marginal.

[24] Figure 6 shows the spatial distribution of remotely sensed GEP for the study area surrounding the flux tower site as 8-d averaged values for the examples of DOY 26–33 (February, Figure 6a), DOY 98–106 (April, Figure 6b), 24–248 (August, Figure 6c) and 288–296 (October, Figure 6d). The highest GEP values were found for the mature forest stands with higher L_e values, while young regeneration sites (following harvesting) had the lowest rates of photosynthesis. Maximum GEP values in February obtained up to 9 μmol m^{-2}s^{-1}, while maximum values in August reached 30 μmol m^{-2} s^{-1}. Structure-related differences in GEP were persistent throughout the year, and were most distinct for higher levels of productivity (i.e., during the summer) with mature stands absorbing significantly more carbon than younger stands. The productivity of

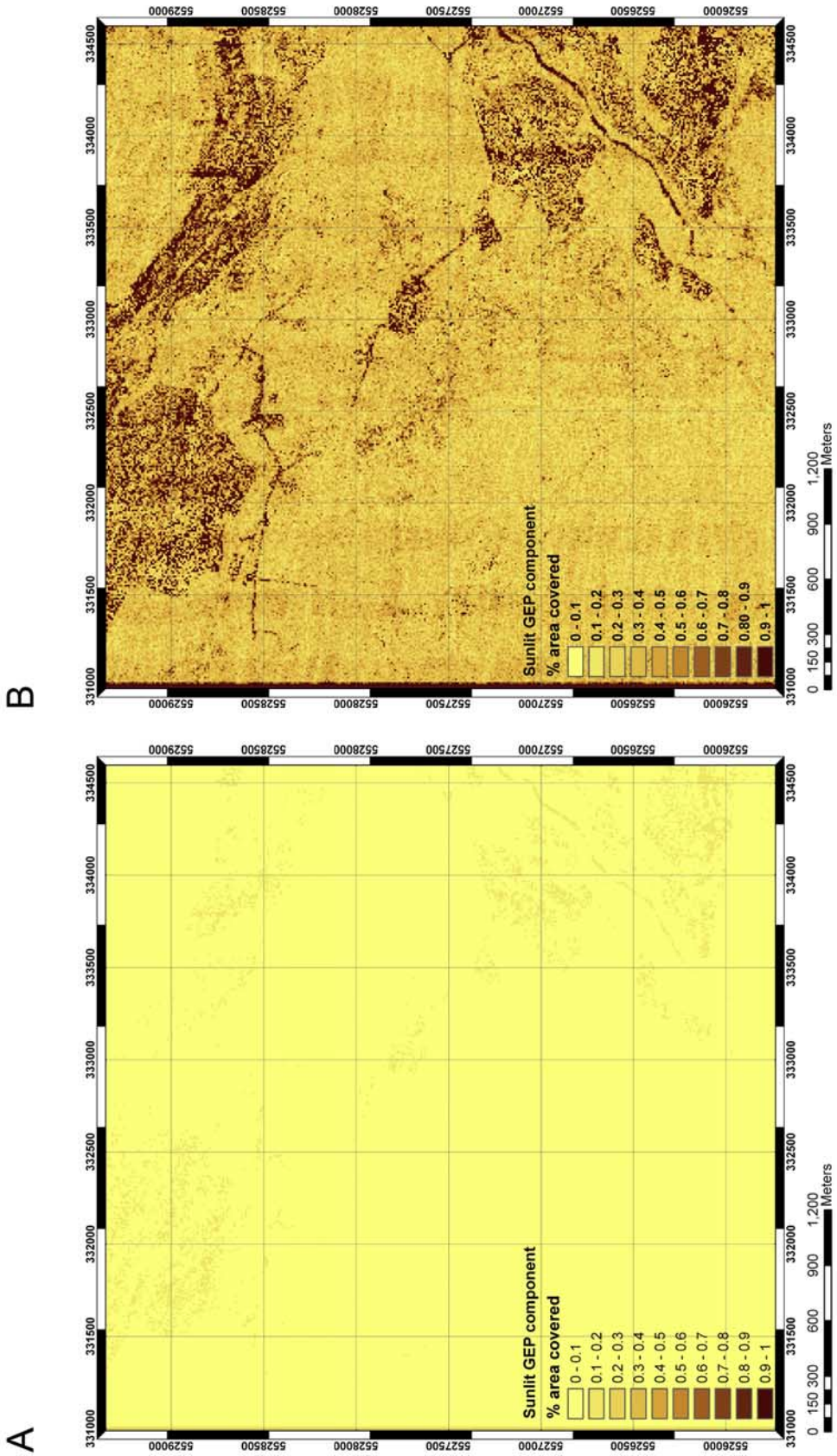

Figure 5. Spatial distribution of sunlit GEP components for (a) a cloudy and (b) a sunny day. The ratio of direct to diffuse radiation was 0.2 and 9, respectively. The different gray tones show the percent coverage of the sunlit GEP component per 10×10 m cell. The coverage of shaded GEP component is the compliment of the images.

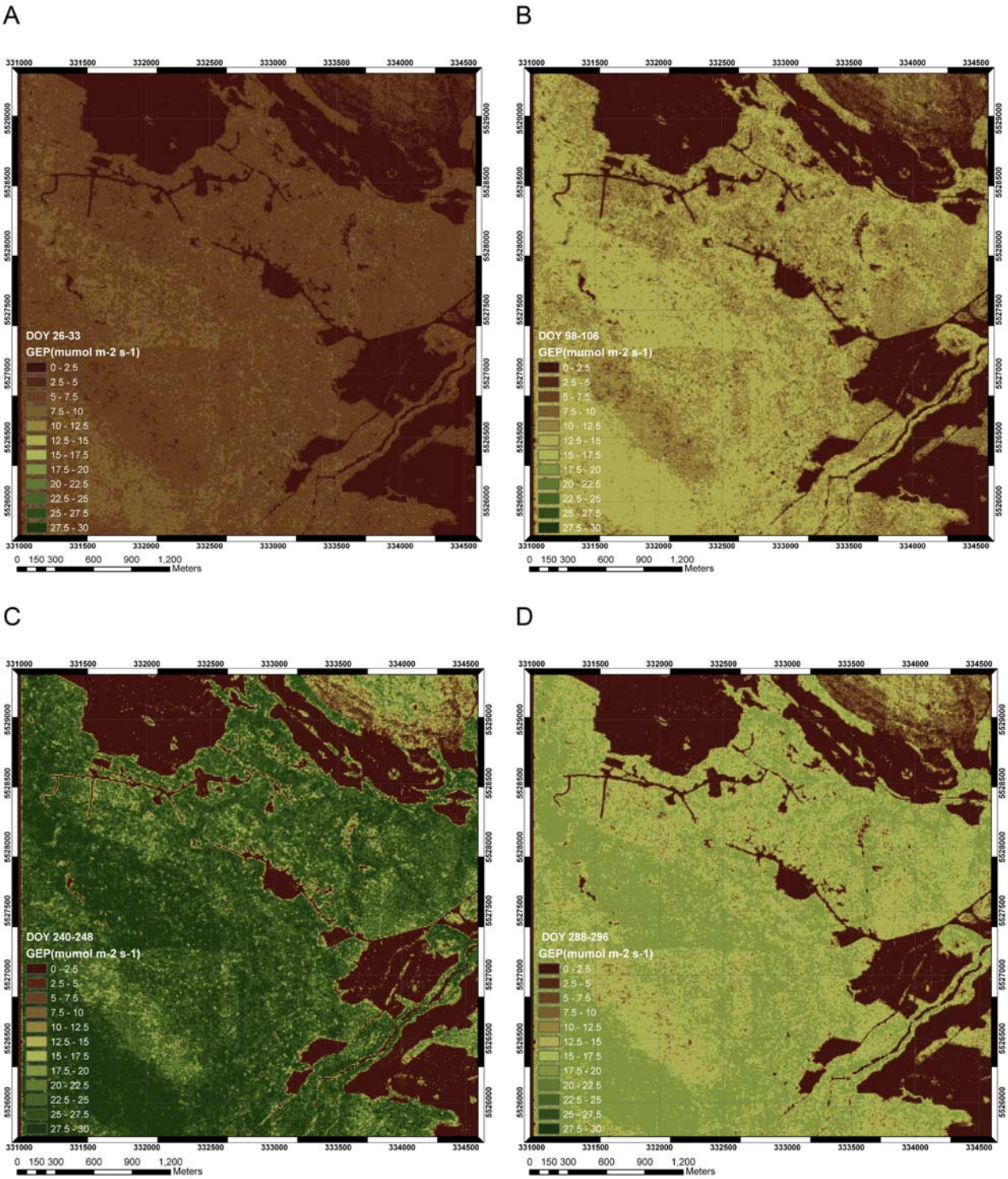

Figure 6. Spatial distribution of GEP (sunlit plus shaded) as a function of canopy structure for the study area, estimated as 8-d averages for the examples of a 8-d time period in (a) late winter (February), (b) early spring (April), (c) late summer (August), and (d) fall (October). The moderate climate conditions allow vegetation to photosynthesize almost year-round [*Morgenstern et al.*, 2004].

non-forested areas estimated from this model is close to zero throughout the year, as the LiDAR derived leaf area for these areas is nearly zero.

4.4. Comparing EC Measured and Remotely Sensed GEP

[25] Figure 7 shows the yearly averaged footprint of daytime EC-flux measurements as modeled using *Chen et*

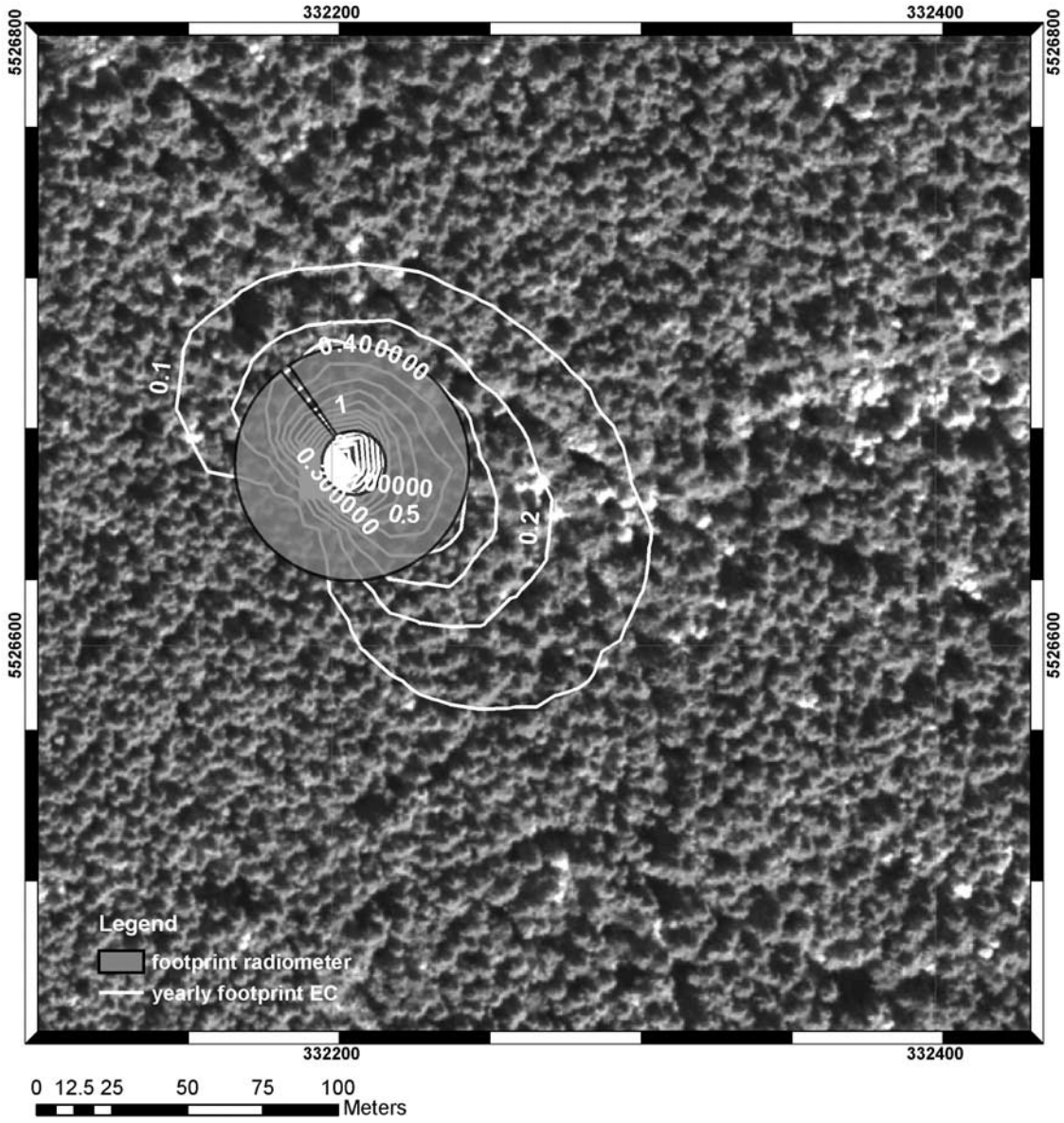

Figure 7. Footprint of the spectro-radiometer (gray) and eddy covariance (EC) data (yearly average between 31 March 2006 and 1 April 2007) over the backdrop of a QuickBird high-resolution satellite image. While the radiometer footprint is constant, the EC footprint varies throughout the year. The contour lines show the different levels of impact (in percent) an area had on the EC measurement over the study period. The figure shows daytime averages only.

al. [2008], overlaid over the footprint of the radiometer instrument installed at the fluxtower. The contour lines show the time-averaged impact (in percent) each 10 m × 10 m cell has on the EC-determined GEP values. The area with a daytime EC-footprint of greater than 0.1% had a diameter of approximately 150 m × 200 m (downwind and crosswind, respectively). As expected, the area with the largest impact was located closest to the tower.

[26] Figure 8 shows a comparison between remotely sensed GEP, weighted the EC footprint (ϕ) versus EC-determined GEP over four 8-d time intervals between 31 March 2006 and 1 April 2007; DOY 26–33 (February, Figure 8a), DOY 98–106 (April, Figure 8b), 24–248 (August, Figure 8c) and 288–296 (October, Figure 8d), in correspondence with Figure 5. All graphs show a high correlation between remotely sensed (predicted) and EC-determined GEP (r^2 = 0.85, 0.91, 0.75 and 0.89, respectively, $p < 0.05$) for the time intervals observed. The slope of the relationship between the remote sensing based model and tower measured GEP showed a maximum deviation of 9% from the 1:1 line.

5. Discussion

[27] This study demonstrated an approach for upscaling remotely sensed GEP to the landscape level by using structural information of the canopy derived from airborne laser scanning, combined with multiangular high spectral

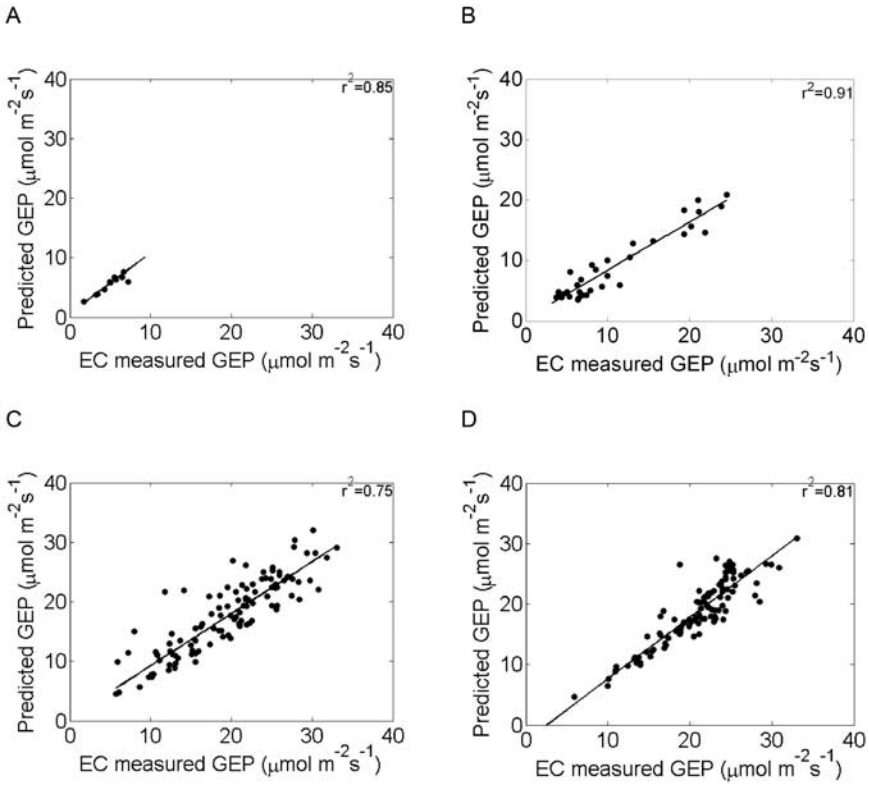

Figure 8. Relationship between remotely sensed GEP, computed using PAR measurements, end-member reflectance of PRI and LiDAR derived information about the canopy structure and GEP measured as using eddy covariance technique. Both data sets are computed over an 8-d period for the examples of (a) late winter (February), (b) early spring (April), (c) late summer (August), and (d) fall (October) (corresponding to Figure 6).

resolution PRI measurements which were decomposed into sunlit and shaded end-members. GEP was predicted vertically and horizontally over a 12 km^2 area at 8-d time steps.

[28] The BRDF approach of *Hilker et al.* [2008a] was successfully used to derive minimal and optimal photosynthetic performance for a given time interval throughout the year. We undertook our analysis at 8-d time steps, comparable to those used by the MODIS GEP product, as it not only provided enough spectral observations for establishing stable reflectance models, but was also flexible enough to account for changing environmental conditions at the research site (Figures 6 and 8). Differences between sunlit and shaded PRI were largely determined by environmental conditions, suggesting that canopy level PRI is a useful indicator for plant stress and thus photosynthetic efficiency. Both sunlit and shaded end-members of PRI revealed a strong relationship with tower measured ε throughout the one year study period (Figure 2). This result is consistent with *Hall et al.* [2008] and *Hilker et al.* [2008a], who showed that ε can be detected at stand scales and under a wide range of view and illumination conditions throughout the year from spectral observations and that changes in ε are largely a result of changes in meteorological conditions [*Hilker et al.*, 2008b]. The slightly higher correlation between the sunlit PRI end-member and ε in comparision to the shaded PRI end-member can be explained by the greater likelihood of the sunlit canopy to be exposed excessive radiation conditions leading to downregulation of photosynthesis. Differences between sunlit and shaded end-members of PRI were greatest under conditions where ε was low as under these conditions the sunlit canopy showed the most distinctive reaction to light saturation.

[29] The approaches of *Lovell et al.* [2003] and *Coops et al.* [2007] were successfully used for modeling the vertical and horizontal distribution of foliage and light interception within the tree canopy over two different-aged forest stands and thus allowed useful predictions of light interception at a landscape level with a high spatial resolution. Largest values for GEP were found in the older stands throughout the year, largely due to a bigger canopy surface, which led to greater absorption of PAR. Our results also demonstrate that diffuse sky radiation plays an important role in forest productivity, even on sunny days, as the diffuse radiation component largely dominates the radiation regime below the top of the canopy. This result is consistent with *Alton et al.* [2007] and *Kotchenova et al.* [2004] finding that within canopy foliage can contribute significantly to stand level GEP. While spectral measurements alone often fail to account for within canopy productivity [*Hall et al.*, 1992], LiDAR has been successfully used for extrapolating top of canopy level reflectance throughout different height levels of the canopy. The LiDAR based model yielded good results for forested areas throughout the year (Figures 6 and 8) the approach, however, is likely to underestimate the productivity of new regeneration areas as the leaf area is only assessed with a vertical resolution of 1 m and LiDAR

returns below this threshold are often, such as in the case of this study, considered ground returns rather than shrub or herbal vegetation. A possible way to mitigate this false estimation is to estimate GEP from surface reflectance directly within these areas.

[30] The spectro-radiometer installed at the site was able to capture the majority of the top of canopy reflectance for the EC-footprint area as estimated using the flux footprint model of *Chen et al.* [2008]. Daytime GEP originated from a relatively restricted area around the tower, but due to the nature of EC-flux measurements, was vertically integrated throughout the canopy. The approach of modeling the within-canopy light regime using LiDAR combined with estimates of ε derived from multiangular top of canopy reflectance measurements yielded accurate predictions of stand level photosynthesis for the time periods observed (Figure 8). Although remotely sensed data did slightly underestimate GEP (Figure 8) due to the simple logarithmic conversion of PRI [*Hilker et al.*, 2008a], which was linearly scaled according to the maximum of EC-determined ε, the slope of the relationship between EC measured and remotely sensed GEP showed less than 10% variation from one (Figure 8). The remote sensing based model was therefore able to yield accurate predictions of GEP at the site for the time periods observed.

[31] The approach described in this study assumes that vegetation stress factors other than light are spatially constant and that the xanthophyll related response to light is constant, which is only reasonable over smaller areas within homogenous environmental conditions. Another assumption is that changes in the pigment pool size (=carotenoid to chlorophyll ratio), were small within each 8-d period and over the study area [*Barton and North*, 2001] and possible age related biochemical differences in foliage composition had only minor effects on PRI. As a result, the area to which spectral measurements can be extrapolated is limited as (1) the empirical relationship between ε and PRI will change with species composition and (2) light independent stress factors such as soil-water or nutrition supply are likely to change with slope soil type and water table thereby affecting PRI. More research will be required to investigate the interactions between of these factors and stand level ε. A further simplifying assumption made in here is that the diffuse radiation component is independent of both mutual shading effects and θ (lambertian leaf surfaces) and thus approximately uniformly distributed within the canopy. This assumption is valid to a first approximation, as the magnitude of the scattering effect of direct radiation within the canopy is small [*Norman*, 1980; *Forseth and Norman*, 1991].

[32] While this study has demonstrated a possibility to extrapolate stand-based findings of GEP to the landscape level at a mature Douglas-fir site, further research is necessary to investigate the potential and limits of this method for different vegetation types and across sites. For example, different canopy structures may yield different relationships between sunlit and shaded PRI components and ε (Figure 2 [*Rahman et al.*, 2001]), with potential implications for the modeling algorithm introduced in this study. For instance, more uniformly distributed deciduous forests in more southern latitudes, may show less distinction between sunlit and shaded PRI end-members, as shading was found to be less important for these forest types [*Rahman et al.*, 2001]. Additionally, multiple studies have demonstrated that the PRI-ε relationship varies with species composition site conditions and leaf pigment concentrations [*Barton and North*, 2001]. As a result, the findings of this study may not be easily transferable across sites. The modeling approach introduced in this study is however, suitable for upscaling canopy level (or even leaf level) observations from tower based spectral observations to small scaled satellite measures around the tower, such as 1km^2 MODIS pixels and does therefore allow a calibration between tower-based and satellite based instrumentation. Tower measured spectra sampled year-round at multiple sites using the existing eddy covariance tower network can therefore be helpful in future efforts trying to relate stand-based GEP measurements with globally available satellite data [*Heinsch et al.*, 2006; *Running et al.*, 2004; *Drolet et al.*, 2005].

6. Conclusions and Implications

[33] Multiangular, high spectral resolution optical remote sensing data are useful for determining stand level photosynthesis. Spectra obtained from such observations can be decomposed into their sunlit and shaded end-members using bidirectional reflectance distribution functions. Simultaneous measurements of the canopy structure, such as demonstrated in this study using LiDAR, will then allow determining the area fraction covered by each of these end-members thereby facilitating an extrapolation of stand level measurements to landscape and satellite observable scales. Tower-based optical remote sensing instruments in combination with airborne LiDAR measurements can therefore be vital components for calibrating high spectral resolution satellite instruments designed to measure landscape and global level photosynthesis from space.

[34] **Acknowledgments.** The LiDAR data for this project was acquired by Benoit St-Onge, of the University of Quebec at Montreal, as part of an ongoing collaborative project with funds provided by the Government of Canada through NSERC and BIOCAP. We would like to thank Dominic Lessard, Rick Ketler, and Andrew Sauter from UBC Faculty of Land and Food Systems (LFS) for their assistance in technical design, installation, and maintenance of the radiometer platform. This research is partially funded by a DAAD postgraduate scholarship to T. Hilker, an NSERC Discovery Grant to N. Coops, and funds provided to UBC from Fluxnet-Canada, NSERC, and BIOCAP.

References

Alton, P. B., P. R. North, and S. O. Los (2007), The impact of diffuse sunlight on canopy light-use efficiency, gross photosynthetic product and net ecosystem exchange in three forest biomes, *Global Change Biol.*, *13*, 776–787.

Annandale, J. G., N. Z. Jovanovic, G. S. Campbell, N. Du Sautoy, and P. Lobit (2002), Two-dimensional solar radiation interception model for hedgerow fruit trees, *Agric. For. Meteorol.*, *121*, 207–225.

Asner, G. P., and A. S. Warner (2003), Canopy shadow in Ikonos satellite observations of tropical forests and savannas, *Remote Sens. Environ.*, *87*, 521–533.

Asner, G. P., C. A. Bateson, J. L. Privette, N. El Saleous, and C. A. Wessman (1998), Estimating vegetation structural effects on carbon uptake using satellite data fusion and inverse modeling, *J. Geophys. Res.*, *103*, 28,839–28,853.

Asrar, G., M. Fuchs, E. Kanemasu, and J. Hatfield (1984), Estimating absorbed photosynthetic radiation and leaf area index from spectral reflectance in wheat, *Agron. J.*, *76*, 300–306.

Barnsley, M. J., P. Lewis, M. Sutherland, and J. P. Muller (1997), Estimating land surface albedo in the Hapex-Sahel southern super-site: Inversion of two BRDF models against multiple angle Asas images, *J. Hydrol. Amsterdam*, *189*, 749–778.

Barton, C. V. M., and P. R. J. North (2001), Remote sensing of canopy light use efficiency using the photochemical reflectance index - Model and sensitivity analysis, *Remote Sens. Environ.*, *78*, 264–273.

Brakke, T. W. (1994), Specular and diffuse components of radiation scattered by leaves, *Agric. For. Meteorol.*, *71*, 283–295.

Chen, B., J. M. Chen, G. Mo, T. A. Black, and D. E. J. Worthy (2008), Comparison of regional carbon flux estimates from CO_2 concentration measurements and remote sensing based footprint integration, *Global Biogeochem. Cycles*, *22*, GB2012, doi:10.1029/2007GB003024.

Chen, J. M. (1996), Canopy architecture and remote sensing of the fraction of photosynthetically active radiation absorbed by boreal conifer forests, *IEEE Trans. Geosci. Remote Sens.*, *34*, 1353–1368.

Chen, J., and T. Black (1991), Measuring leaf area index of plant canopies with branch architecture, *Agric. For. Meteorol.*, *57*, 1–12.

Chen, J. M., J. Liu, S. G. Leblanc, R. Lacaze, and J. L. Roujean (2003), Multi-angular optical remote sensing for assessing vegetation structure and carbon absorption, *Remote Sens. Environ.*, *84*, 516–525.

Chen, J. M., A. Govind, O. Sonnentag, Y. Q. Zhang, A. Barr, and B. Amiro (2006), Leaf area index measurements at Fluxnet-Canada forest sites, *Agric. For. Meteorol.*, *140*, 257–268.

Coops, N. C., T. Hilker, M. A. Wulder, B. St-Onge, G. Newnham, A. Siggins, and J. A. Trofymow (2007), Estimating canopy structure of Douglas-fir forest stands from discrete-return lidar, *Trees Structure Function*, *21*, 295–310.

Daughtry, C. S. T., K. P. Gallo, and M. E. Bauer (1983), Spectral estimates of solar-radiation intercepted by corn canopies, *Agron. J.*, *75*, 527–531.

Demmig-Adams, B., and W. W. Adams (2000), Photosynthesis - Harvesting sunlight safely, *Nature*, *403*, 371–372.

Demmig-Adams, B., D. L. Moeller, B. A. Logan, and W. W. Adams (1998), Positive correlation between levels of retained Zeaxanthin plus Antheraxanthin and degree of photoinhibition in shade leaves of Schefflera Arboricola (Hayata) Merrill, *Planta*, *205*, 367–374.

Drolet, G. G., K. F. Huemmrich, F. G. Hall, E. M. Middleton, T. A. Black, A. G. Barr, and H. A. Margolis (2005), A Modis-derived photochemical reflectance index to detect inter-annual variations in the photosynthetic light-use efficiency of a boreal deciduous forest, *Remote Sens. Environ.*, *98*, 212–224.

Eck, T. F., and D. G. Dye (1991), Satellite estimation of incident photosynthetically active radiation using ultraviolet reflectance, *Remote Sens. Environ.*, *38*, 135–146.

Forseth, I. N., and J. M. Norman (1991), Modelling of solar irradiance, leaf energy budget, and canopy photosynthesis, in *Techniques in Photosynthesis and Productivity Research for a Changing Environment*, edited by D. O. Hall et al., Chapman and Hall, London.

Gamon, J. A., C. B. Field, W. Bilger, O. Bjorkman, A. L. Fredeen, and J. Penuelas (1990), Remote-sensing of the xanthophyll cycle and chlorophyll fluorescence in sunflower leaves and canopies, *Oecologia*, *85*, 1–7.

Gamon, J. A., J. Penuelas, and C. B. Field (1992), A narrow-waveband spectral index that tracks diurnal changes in photosynthetic efficiency, *Remote Sens. Environ.*, *41*, 35–44.

Gamon, J. A., I. Filella and J. Peñuelas (1993), The dynamic 531-nanometer reflectance signal: A survey of twenty angiosperm species, in *Photosynthetic Responses to the Environment*, edited by H. Y. Yamamoto and C. M. Smith, pp. 172–177, Am. Soc. of Plant Physiol, Rockville.

Gao, F., C. B. Schaaf, A. H. Strahler, Y. Jin, and X. Li (2003), Detecting vegetation structure using a kernel-based Brdf model, *Remote Sens. Environ.*, *86*, 198–205.

Goodwin, G. (1937), Regeneration study on the logged-off lands of the Comox Logging and Railway Company Oyster River forest survey, *R 72, Surv. File 0124780,* 39 pp. and map, B. C. For. Serv., Canada.

Grace, J., et al. (2007), Can we measure terrestrial photosynthesis from space directly, using spectral reflectance and fluorescence?, *Global Change Biol.*, *13*, 1484–1497.

Hall, F. G., K. F. Huemmrich, and S. N. Goward (1990), Use of narrow-band spectra to estimate the fraction of absorbed photosynthetically active radiation, *Remote Sens. Environ.*, *32*, 47–54.

Hall, F. G., K. F. Huemmrich, S. J. Goetz, P. J. Sellers, and J. E. Nickeson (1992), Satellite remote-sensing of surface-energy balance: Success, failures, and unresolved issues in Fife, *J. Geophys. Res.*, *97*, 19,061–19,089.

Hall, F. G., J. R. Townshend, and E. T. Engman (1995a), Status of remote-sensing algorithms for estimation of land-surface state parameters, *Remote Sens. Environ.*, *51*, 138–156.

Hall, F. G., Y. E. Shimabukuro, and K. F. Huemmrich (1995b), Remote sensing of forest biophysical structure using mixture decomposition and geometric reflectance models, *Ecol. Appl.*, *5*, 993–1013.

Hall, F. G., T. Hilker, N. C. Coops, A. Lyapustin, F. Huemmrich, E. Middleton, H. Margolis, G. Drolet, and T. Black (2008), Multi-angle remote sensing of forest light use efficiency by observing PRI variation with canopy shadow fraction, *Remote Sens. Environ.*, *112*, 3201–3211.

Heinsch, F. A., et al. (2006), Evaluation of remote sensing based terrestrial productivity from Modis using regional tower eddy flux network observations, *IEEE Trans. Geosci. Remote Sens.*, *44*, 1908–1925.

Hilker, T., N. C. Coops, Z. Nesic, M. A. Wulder, and A. T. Black (2007), Instrumentation and approach for unattended year-round tower based measurements of spectral reflectance, *Comput. Electron. Agric.*, *56*, 72–84.

Hilker, T., N. C. Coops, F. G. Hall, T. A. Black, M. A. Wulder, Z. Nesic, and P. Krishnan (2008a), Separating physiologically and directionally induced changes in PRI using BRDF models, *Remote Sens. Environ.*, *112*, 2777–2788.

Hilker, T., N. C. Coops, C. R. Schwalm, R. S. Jassal, T. A. Black, and P. Krishnan (2008b), Effects of mutual shading of tree crowns on prediction of photosynthetic light use efficiency in a coastal Douglas fir forest, *Tree Physiol.*, *28*, 825–834.

Humphreys, E. R., T. A. Black, K. Morgenstern, T. B. Cai, G. B. Drewitt, Z. Nesic, and J. A. Trofymow (2006), Carbon dioxide fluxes in coastal Douglas-fir stands at different stages of development after clearcut harvesting, *Agric. For. Meteorol.*, *140*, 6–22.

Jassal, R. S., T. A. Black, T. B. Cai, K. Morgenstern, Z. Li, D. Gaumont-Guay, and Z. Nesic (2007), Components of ecosystem respiration and an estimate of net primary productivity of an intermediate-aged Douglas-fir stand, *Agric. For. Meteorol.*, *144*, 44–57.

Kormann, R., and F. X. Meixner (2001), An analytical footprint model for non-neutral stratification, *Boundary Layer Meteorol.*, *99*, 207–224.

Kotchenova, S. Y., X. D. Song, N. V. Shabanova, C. S. Potter, Y. Knyazikhin, and R. B. Myneni (2004), Lidar remote sensing for modeling gross primary production of deciduous forests, *Remote Sens. Environ.*, *92*, 158–172.

Leclerc, M. Y., and G. W. Thurtell (1990), Footprint prediction of scalar fluxes using a Markovian analysis, *Boundary Layer Meteorol.*, *52*, 247–258.

Lefsky, M. A., D. P. Turner, M. Guzy, and W. B. Cohen (2005), Combining lidar estimates of aboveground biomass and Landsat estimates of stand age for spatially extensive validation of modeled forest productivity, *Remote Sens. Environ.*, *95*, 549–558.

Li, X., and A. Strahler (1985), Geometric-optical modeling of a conifer forest canopy, *IEEE Trans. Geosci. Remote Sens.*, *23*, 705–721.

Li, X., and A. Strahler (1992), Geometric-optical bidirectional reflectance modeling of the discrete crown vegetation canopy–Effect of crown shape and mutual shadowing, *IEEE Trans. Geosci. Remote Sens.*, *30*, 276–292.

Los, S. O., P. R. J. North, W. M. F. Grey, and M. J. Barnsley (2005), A method to convert AVHRR normalized difference vegetation index time series to a standard viewing and illumination geometry, *Remote Sens. Environ.*, *99*, 400–411.

Lovell, J. L., D. L. B. Jupp, D. S. Culvenor, and N. C. Coops (2003), Using airborner and ground-based ranging lidar to measure canopy structure in Australian forests, *Can. J. Rem. Sens.*, *29*, 607–622.

Magnussen, S., and P. Boudewyn (1998), Derivations of stand heights from airborne laser scanner data with canopy-based quantile estimators, *Can. J. For. Res.*, *28*, 1016–1031.

Middleton, E. M., D. W. Deering, and S. P. Ahmad (1987), Surface anisotropy and hemispheric reflectance for a semiarid ecosystem, *Remote Sens. Environ.*, *23*, 193–212.

Monteith, J. L. (1972), Solar-radiation and productivity in tropical ecosystems, *J. Appl. Ecol.*, *9*, 747–766.

Monteith, J. L. (1977), Climate and efficiency of crop production in Britain, *Philos. Trans. R. Soc. London, Ser. B, Biol. Sci.*, *281*, 277–294.

Morgenstern, K., T. A. Black, E. R. Humphreys, T. J. Griffis, G. B. Drewitt, T. B. Cai, Z. Nesic, D. L. Spittlehouse, and N. J. Livingstone (2004), Sensitivity and uncertainty of the carbon balance of a Pacific Northwest Douglas-fir forest during an El Nino La Nina cycle, *Agric. For. Meteorol.*, *123*, 201–219.

Myneni, R. B., et al. (2002), Global products of vegetation leaf area and fraction absorbed par from year one of Modis data, *Remote Sens. Environ.*, *83*, 214–231.

Næsset, E. (1997), Determination of mean tree height of forest stands using airborne laser scanner data, *ISPRS J. Photogramm. Remote Sens.*, *52*, 49–56.

Næsset, E. (2002), Predicting forest stand characteristics with airborne scanning laser using a practical two-stage procedure and field data, *Remote Sens. Environ.*, *80*, 88–99.

Næsset, E., and T. Økland (2002), Estimating tree height and tree crown properties using airborne scanning laser in a boreal nature reserve, *Remote Sens. Environ.*, *79*, 105–115.

Nichol, C. J., J. Lloyd, O. Shibistova, A. Arneth, C. Roser, A. Knohl, S. Matsubara, and J. Grace (2002), Remote sensing of photosynthetic-light-use efficiency of a Siberian boreal forest, *Tellus*, *54*, *Ser. B*, 677–687.

Norman, J. M. (1980), Interfacing leaf and canopy light interception models, in *Predicting Photosynthesis for Ecosystem Models*, edited by J. D. Hesketh and J. W. Jones, pp. 49–67, CRC Press, Boca Raton, Fla.

Peddle, D. R., F. G. Hall, and E. F. Ledrew (1999), Spectral mixture analysis and geometric-optical reflectance modeling of boreal forest biophysical structure, *Remote Sens. Environ.*, *67*, 288–297.

Persson, A., J. Holmgren, and U. Soderman (2002), Detecting and measuring individual trees using an airborne laser scanner, *Photogramm. Eng. Remote Sens.*, *68*, 925–932.

Prince, S. D., and S. N. Goward (1995), Global primary production: A remote sensing approach, *J. Biogeogr.*, *22*, 815–835.

Rahman, A. F., J. A. Gamon, D. A. Fuentes, D. A. Roberts, and D. Prentiss (2001), Modeling spatially distributed ecosystem flux of boreal forest using hyperspectral indices from Aviris imagery, *J. Geophys. Res.*, *106*, 33,579–33,591.

Rahman, A. F., D. A. Sims, V. D. Cordova, and B. Z. El-Masri (2005), Potential of Modis Evi and surface temperature for directly estimating per-pixel ecosystem C fluxes, *Geophys. Res. Lett.*, *32*, L19404, doi:10.1029/2005GL024127.

Reda, I., and A. Andreas (2004), Solar position algorithm for solar radiation applications, *Sol. Energy*, *76*, 577–589.

Roujean, J. L., M. Leroy, and P. Y. Deschamps (1992), A bidirectional reflectance model of the Earth's surface for the correction of remote-sensing data, *J. Geophys. Res.*, *97*, 20,455–20,468.

Running, S. W., D. D. Baldocchi, D. P. Turner, S. T. Gower, P. S. Bakwin, and K. A. Hibbard (1999), A global terrestrial monitoring network integrating tower fluxes, flask sampling, ecosystem modeling and Eos satellite data, *Remote Sens. Environ.*, *70*, 108–127.

Running, S. W., R. R. Nemani, F. A. Heinsch, M. S. Zhao, M. Reeves, and H. Hashimoto (2004), A continuous satellite-derived measure of global terrestrial primary production, *BioScience*, *54*, 547–560.

Schmid, H. P., and C. R. Lloyd (1999), Spatial representativeness and the location bias of flux footprints over inhomogeneous areas, *Agric. For. Meteorol.*, *93*, 195–209.

Sellers, P. (1985), Canopy reflectance, photosynthesis and transpiration, *Int. J. Remote Sens.*, *6*, 1335–1372.

Sellers, P. J. (1987), Canopy reflectance, photosynthesis, and transpiration. 2. The role of biophysics in the linearity of their interdependence, *Remote Sens. Environ.*, *21*, 143–183.

Sellers, P. J., and F. G. Hall (1992), Fife in 1992: Results, scientific gains, and future-research directions, *J. Geophys. Res.*, *97*, 19,091–19,109.

Sellers, P. J., et al. (1995), Remote-sensing of the land-surface for studies of global change - Models, algorithms, experiments, *Remote Sens. Environ.*, *51*, 3–26.

Sellers, P. J., D. A. Randall, G. J. Collatz, J. A. Berry, C. B. Field, D. A. Dazlich, C. Zhang, G. D. Collelo, and L. Bounoua (1996a), A revised land surface parameterization (Sib2) for atmospheric GCMs. 1. Model formulation, *J. Clim.*, *9*, 676–705.

Sellers, P. J., S. O. Los, C. J. Tucker, C. O. Justice, D. A. Dazlich, G. J. Collatz, and D. A. Randall (1996b), A revised land surface parameterization (Sib2) for atmospheric GCMs. 2. The generation of global fields of terrestrial biophysical parameters from satellite data, *J. Clim.*, *9*, 706–737.

Sellers, P. J., et al. (1997), Boreas in 1997: Experiment overview, scientific results, and future directions, *J. Geophys. Res.*, *102*, 28,731–28,769.

Smolander, S., and P. Stenberg (2001), A method for estimating light interception by a conifer shoot, *Tree Physiol.*, *21*, 797–803.

Tucker, C. (1979), Red and photographic infrared linear combinations for monitoring vegetation, *Remote Sens. Environ.*, *8*, 127–150.

Tucker, C., and P. Sellers (1986), Satellite remote sensing of primary production, *Int. J. Remote Sens.*, *7*, 1395–1416.

Tucker, C. J., W. H. Jones, W. A. Kley, and G. J. Sundstrom (1981), A 3-band hand-held radiometer for field use, *Science*, *211*, 281–283.

Turner, D. P., S. Urbanski, D. Bremer, S. C. Wofsy, T. Meyers, S. T. Gower, and M. Gregory (2003), A cross-biome comparison of daily light use efficiency for gross primary production, *Global Change Biol.*, *9*, 383–395.

Van Laake, P. E., and G. A. Sanchez-Azofeifa (2004), Simplified atmospheric radiative transfer modelling for estimating incident PAR using Modis atmosphere products, *Remote Sens. Environ.*, *91*, 98–113.

Wanner, W., X. Li, and A. Strahler (1995), On the derivation of kernels for kernel-driven models of bidirectional reflectance, *J. Geophys. Res.*, *100*, 21,077–21,089.

Weiss, A., and J. M. Norman (1985), Partitioning solar-radiation into direct and diffuse, visible and near-infrared components, *Agric. For. Meteorol.*, *34*, 205–213.

Wulder, M. (1998), Optical remote sensing techniques for the assessment of forest inventory and biophysical parameters, *Prog. Phys. Geogr.*, *22*, 449–476.

T. A. Black and B. Chen, Faculty of Land and Food Systems, University of British Columbia, 2357 Main Mall, Vancouver, BC V6T 1Z4, Canada.

N. C. Coops and T. Hilker, Faculty of Forest Resources Management, University of British Columbia, 2424 Main Mall, Vancouver, BC V6T 1Z4, Canada. (thilker@interchange.ubc.ca)

F. G. Hall, Joint Center for Earth Systems Technology, University of Maryland, Baltimore County, Goddard Space Flight Center, Code 614.4, Greenbelt, MD 20771, USA.

K. F. Huemmrich, Joint Center for Earth Systems Technology, University of Maryland, Baltimore County, Catonsville, MD 21228, USA.

P. Krishnan, Atmospheric Turbulence and Diffusion Division, National Oceanic and Atmospheric Administration, 456 S. Illinois Avenue, Oak Ridge, TN 37830, USA.

E. M. Middleton, Biospheric Sciences Branch, Code 614.4, NASA Goddard Space Flight Center, Greenbelt, MD 20771, USA.

P. J. Sellers, Lyndon B. Johnson Space Center, Houston, TX 77058, USA.

M. A. Wulder, Canadian Forest Service (Pacific Forestry Centre), Natural Resources Canada, 506 West Burnside Road, Victoria, BC V8Z 1M5, Canada.